Supporting Information

A Fast Alternative to the Galvanostatic Intermittent Titration Technique

Yu-Chuan Chien[a], Haidong Liu[a], Ashok S. Menon[a], William R. Brant[a], Daniel Brandell[a,*], Matthew J. Lacey[b,*]

[a]Department of Chemistry—Ångström Laboratory, Uppsala University,

Box 538, Lägerhyddsvägen 1, 751 21 Uppsala, Sweden

[b]Scania CV AB, 151 87 Södertälje, Sweden

Table of Contents

1. Full solution to Fick's Second Law

Equations 1, 2 and 3 in the manuscript can be transformed to spherical coordinates as the following, with n = 1 for Li-ions:

$$\frac{\partial C(r,t)}{\partial t} = \frac{1}{r^2} D \frac{\partial}{\partial r} r^2 \frac{\partial C(r,t)}{\partial r} \quad S1$$

$$\begin{cases} -D\dfrac{\partial C}{\partial r} = \dfrac{I}{FA} \\ C(r,0) = C_0 \end{cases} \quad S2$$

The above has been solved previously[1–4] and is summarized[5,6] as follows for the surface concentration of an electrode particle with a radius r_p:

$$c(r_p,t) = C_0 - \frac{Ir_p}{FAD} f\left(\frac{Dt}{r_p^2}\right) \quad S3$$

where f is defined as follows:

$$f(x) = 3x + 0.2 - 2\sum_{m=1}^{\infty} \frac{1}{\alpha_m^2} e^{-\alpha_m^2 x} \quad S4$$

where, α_m are the positive roots of $\alpha = \tan(\alpha)$, which is listed elsewhere.[3] $f(x)$ has asymptotes in both positive and negative directions. Within 5% error, equation S3 can be approximated by the following:

$$f(x) = \begin{cases} \dfrac{2}{\sqrt{\pi}}\sqrt{x}, & x < 0.0032 \\ 3x + 0.2, & x > 1.27 \end{cases} \quad S5$$

It can be observed that when x < 0.0032, equation S3 can be reduced to

$$C(r_p,t) = C_0 - \frac{2I\sqrt{t}}{FA\sqrt{D\pi}} \quad S6$$

which is the same as Equation 5 in the manuscript.

2. Limit of the current interruption time (Δt) of an ICI measurement

As demonstrated in section 2.2 in the manuscript, the ICI method is derived on the assumption that $F(\tau_1+\Delta t) \approx F(\tau_1)$ in Equation 12. Suppose a relative error of δ is allowed, the two terms should satisfy the following;

$$1-\frac{F(\tau_1)}{F(\tau_1+\Delta t)} < \delta \quad or \quad \frac{F(\tau_1)}{F(\tau_1+\Delta t)} > 1-\delta \qquad S7$$

From equation S3, it is known that

$$F(t) = -\frac{Ir_p}{FAD} f\left(\frac{Dt}{r_p^2}\right) \qquad S8$$

where, the function and parameters are explained previously. The error can be discussed in terms of both asymptotes of f in Equation S5 since the values are bounded by the asymptotes, which can be found out by plotting the function. Thus, for $\tau_1 < 0.0032 r_p^2/D$,

$$F(t) = -\frac{2I}{FA\sqrt{\pi D}}\sqrt{t} \qquad S9$$

$$1-\delta < \frac{\sqrt{\tau_1}}{\sqrt{\tau_1+\Delta t}} \qquad S10$$

$$\rightarrow \Delta t < \frac{(2\delta-\delta^2)}{(1-\delta)^2}\tau_1 \qquad S11$$

Let, $\delta = 0.03$, $\tau_1 = 600$ s. The maximum Δt is around 37 s.

For $\tau_1 > 1.27 r_p^2/D$,

$$F(t) = -\frac{I}{FA}\left(\frac{3t}{r_p}+\frac{r_p}{5D}\right) \qquad S12$$

$$(1-\delta) < \frac{\frac{3\tau_1}{r_p}+\frac{r_p}{5D}}{\frac{3\tau_1+3\Delta t}{r_p}+\frac{r_p}{5D}} \qquad S13$$

$$\rightarrow \Delta t < \frac{\delta}{1-\delta}\left(\tau_1+\frac{r_p^2}{15D}\right) \qquad S14$$

With $\delta = 0.03$, $\tau_1 = 600$ s, $r_p = 2$ μm and $D = 10^{-11}$ cm^2 s^{-1}. The maximum Δt is around 26 s.

Since the $\tau_1 > 1.27 r_p^2/D$ is more likely and Equation S12 is stricter than Equation S10, considering only Equation S12 is sufficient in most cases. Nonetheless, in either case, the $\Delta t = 5$ s in the ICI analysis of this work should be considerably below the limit.

It is worth noting that in the standard ICI protocol, the current is only stopped for a few seconds at a time, in contrast to GITT. Therefore, the limit of Δt increases over the number of measurements in the same course of charge or

discharge since, τ_1 can be effectively accumulated due to the transient current pauses. The limit of Δt discussed above is thus a conservative estimation for the standard ICI protocol.

3. Determination of data collection intervals for $dE/d\sqrt{t}$

With Equation S5, the impact of the choice of data selection interval for the GITT analyses can be examined. With r = 2 µm (average particle radius) and D = 10^{-11} cm^2 s^{-1}, the maximum t is 12.8 s. However, if only potential measurements within 12.8 s are selected, the linear regression renders very large standard deviations due to the limited number of data points. Therefore, the upper limit of the interval is set at 40 s after confirming that the E-$\sqrt{t}$ plots remain linear. The lower limit is set at 5 s since there is a transition region before the linear region on some of the E-$\sqrt{t}$ plots, as reported in previous GITT works on $LiNi_{0.5}Mn_{0.3}Co_{0.2}O_2$ (NMC523).[5] This transition region is prolonged below 3.7 V, as shown in Figure S1(a). The phenomenon is also observed in EIS measurements in this work and in the literature (for $LiNi_{0.33}Mn_{0.33}Co_{0.33}O_2$, NMC111),[7,8] where the Warburg element shifts to lower frequencies. Thus, as the cell is discharged below 3.7 V, the linear region on the E-$\sqrt{t}$ plots shifts to 50–150 s. The semi-infinite diffusion assumption still holds here because D is significantly lower here. The situation is more complicated when the cell is charged in the same SoC because the transition region is still long, but D derived from 50–150 s is around $5 \cdot 10^{-11}$ cm^2 s^{-1}, which makes 150 s considerably long for the semi-infinite diffusion assumption. Therefore, fitting the data to the full solution in S3 is necessary to derive the diffusion coefficient at SoC below 3.7 V upon charging.

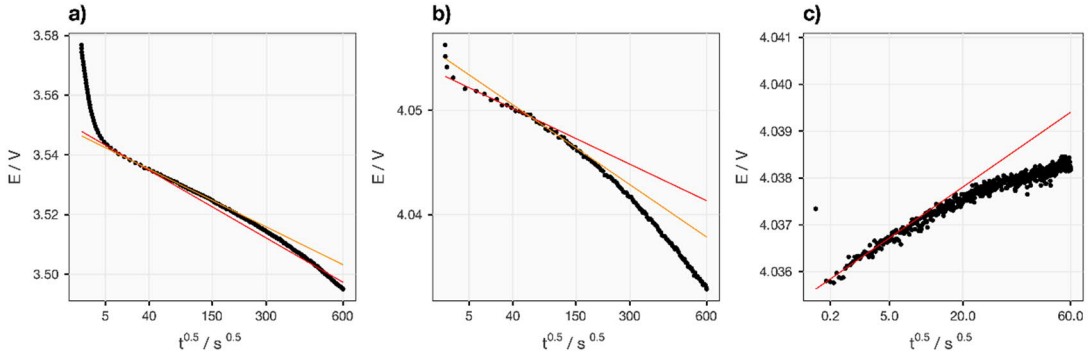

Figure S1. Examples of GITT measurements below 3.7 V (a) and above 3.7 V (b) analyzed by selecting the datapoints in 5–40 s (red) and 50–150 s (orange) intervals. (c) is an example of an ICI measurement following the GITT measurement in (b).

4. Equivalent circuit model and selected impedance spectra

The impedance spectra above 3.7 V were fitted to the equivalent circuit model (ECM) in Figure S2. The ECM is adopted from a previous work on NMC111[8] but the finite-space Warburg element is substituted here by a semi-infinite Warburg element because the spectra here, with the lowest frequency at 10 mHz, do not show a vertical tail. The spectra below 3.7 V show enlarged second semicircle (R2 and CPE2) and do not possess sufficient data points to fit the Warburg element, as shown in Figure S4. Some spectra between 3.6 and 3.7 V from cell 2 can be fitted to the ECM but majority of the spectra from cell 2 show a depressed Warburg element, which is discussed in the section 6. Complete set of impedance spectra can be found via Zenodo.[9]

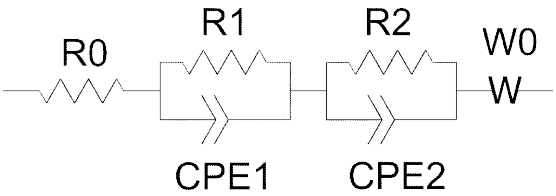

Figure S2. The equivalent circuit model used to fit the impedance spectra above 3.7 V. Details of the interpretation of the model are stated in the source of the model.[8]

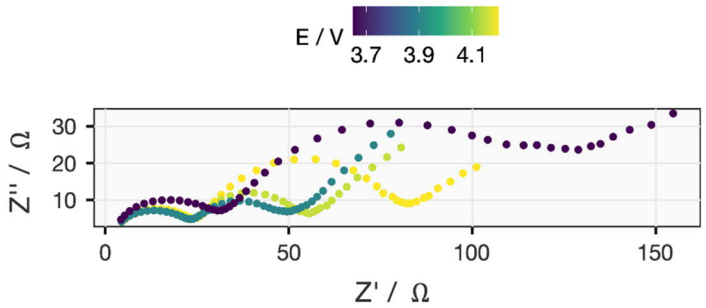

Figure S3. Selected impedance spectra above 3.7 V from the first discharge of cell 1.

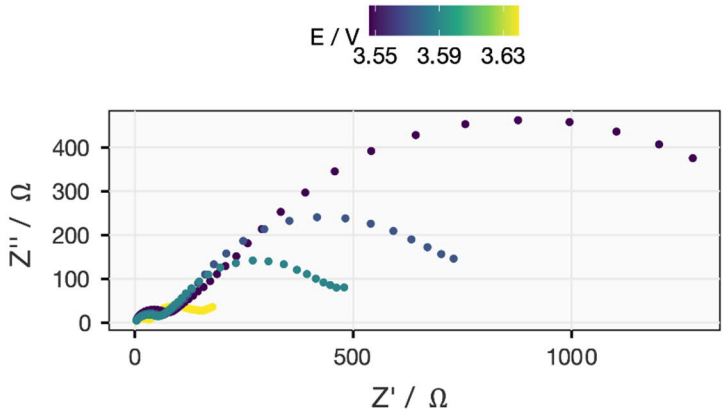

Figure S4. Selected impedance spectra below 3.7 V from the first discharge of cell 1.

5. Relative difference between the results from the GITT and ICI methods

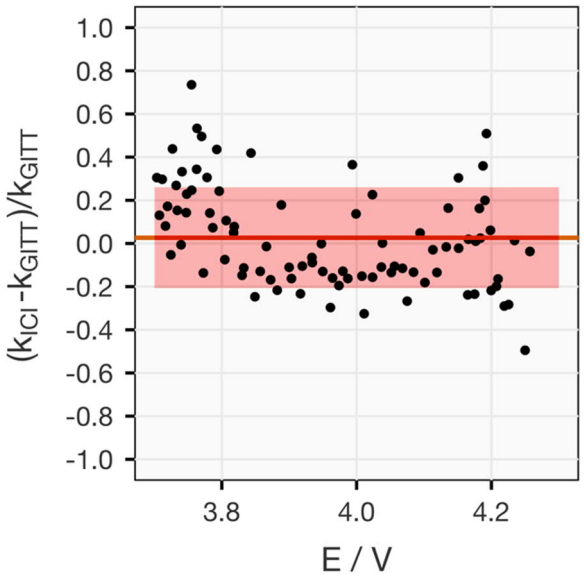

Figure S5. The relative difference between the *k* values from the GITT and ICI methods (k_{GITT} and k_{ICI}, respectively) above 3.7 V in Figure 2 plotted against the OCP of the electrode (E) against Li/Li^+. The average, 0.026, is shown by the horizontal line and the standard deviation, 0.23, is shown by the height of the shaded area above and below the average value.

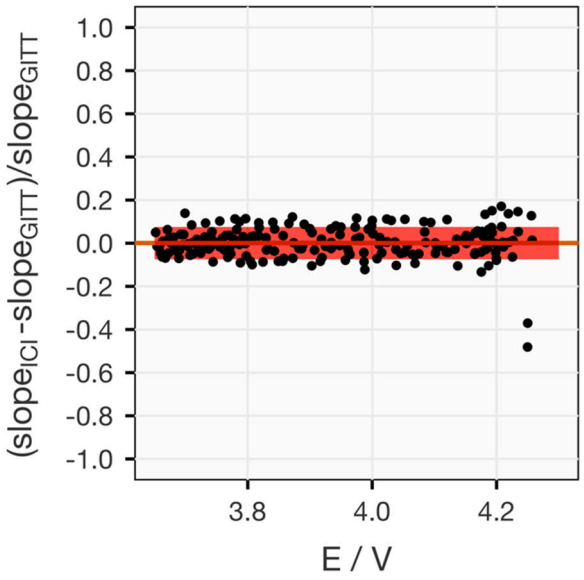

Figure S6. The relative difference between the slope of the OCP (denoted as dE_{OC}/dt_I in Figure 3) from the GITT and ICI methods ($slope_{GITT}$ and $slope_{ICI}$, respectively) above 3.65 V in Figure 3 plotted against the OCP of the electrode (E) against Li/Li^+. The average, 0.000045, is shown by the horizontal line and the standard deviation, 0.086, is shown by the height of the shaded area above and below the average value.

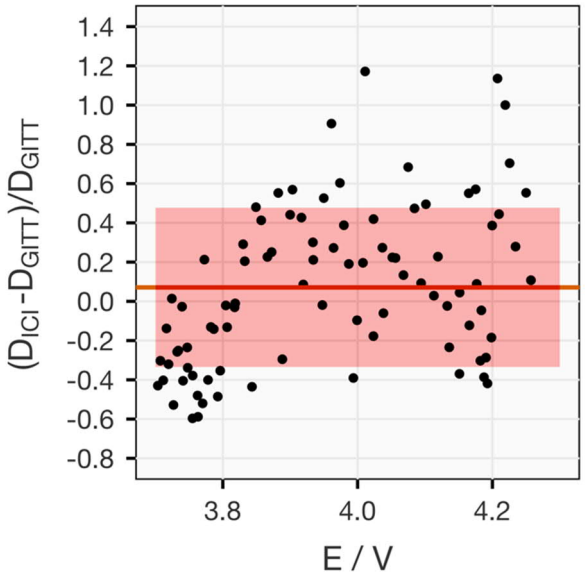

Figure S7. The relative difference between the Li-ion diffusion coefficient in NMC811 from the GITT and ICI methods (D_{GITT} and D_{ICI}, respectively) above 3.7 V in Figure 4 plotted against the OCP of the electrode (E) against Li/Li^+. The average, 0.071, is shown by the horizontal line and the standard deviation, 0.41, is shown by the height of the shaded area above and below the average value.

6. Data from both cells in both cycles

The chemical diffusion coefficient of Li-ions (*D*), diffusion resistance coefficient (*k*) and internal resistance (*R*) obtained by the GITT, ICI method and EIS are presented below. The results of the first cycle of cell 1 is also plotted to facilitate the comparison between the data. The comparison between OCP and pseudo-OCP of cell 2 is also shown. The Warburg element in majority of the impedance spectra from cell 2 does not show a 45° phase angle and is substantially depressed (~22.5°). Therefore, the resulting *k* and *R* from the EIS fittings of cell 2 should be interpreted with caution.

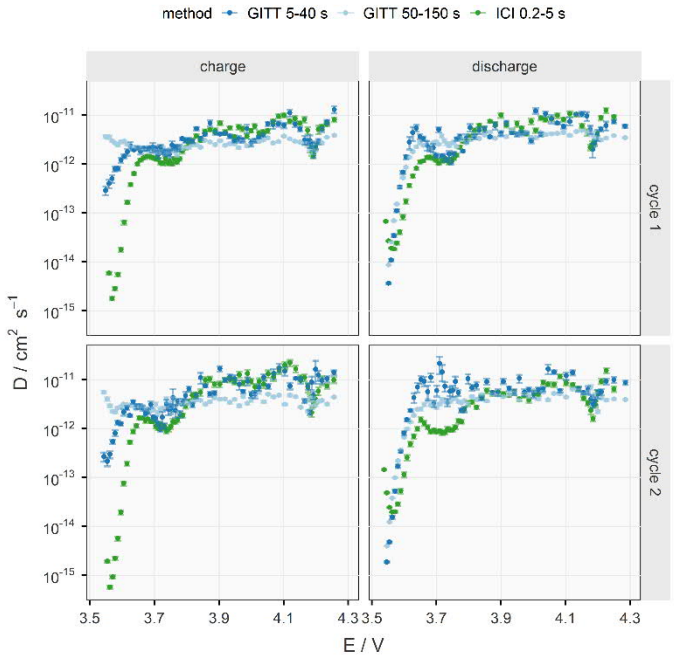

Figure S8. The Li-ion diffusion coefficient in NMC811(D) in cell 1 at various OCP of the electrode (E) against Li/Li^+ derived from the GITT with data selection interval 5–40 s and 50–150 s, the ICI method with data selection interval 0.2–5 s.

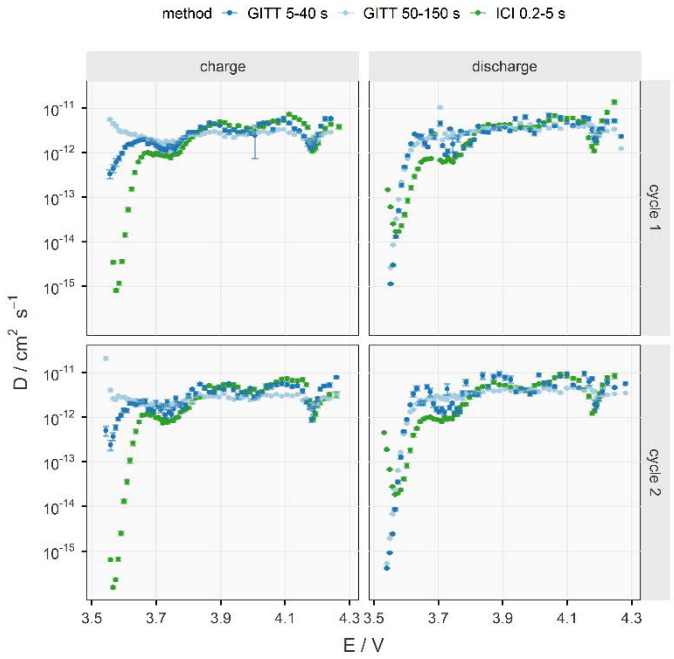

Figure S9. The Li-ion diffusion coefficient in NMC811(D) in cell 2 at various OCP of the electrode (E) against Li/Li$^+$ derived from the GITT with data selection interval 5–40 s and 50–150 s, the ICI method with data selection interval 0.2–5 s.

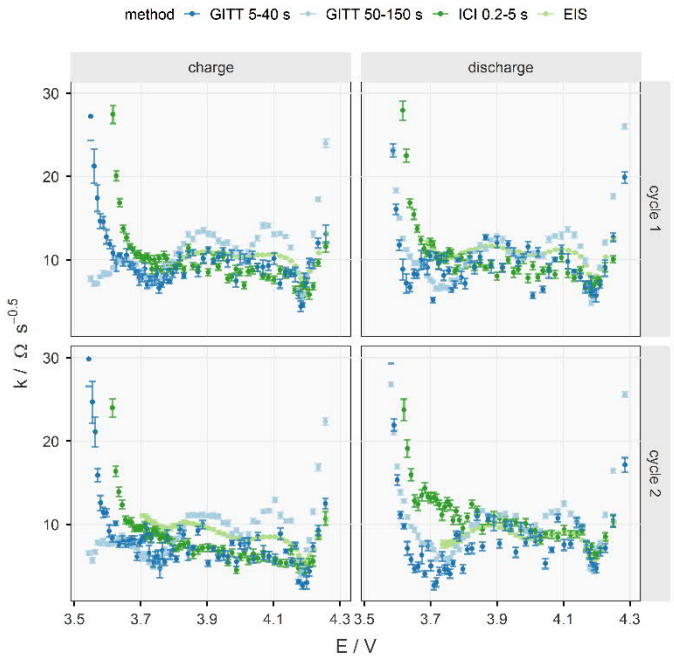

Figure S10. The diffusion resistance coefficient (k) in NMC811(D) in cell 1 at various OCP of the electrode (E) against Li/Li$^+$ derived from the GITT with data selection interval 5–40 s and 50–150 s, the ICI method with data selection interval 0.2–5 s and the EIS fitting ($k = \sigma\sqrt{8/\pi}$, σ: Warburg coefficient).

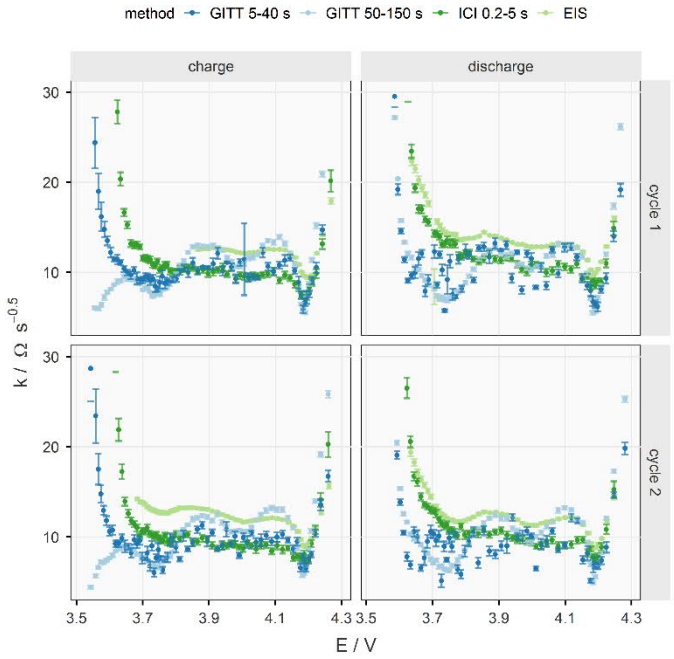

Figure S11. The diffusion resistance coefficient (k) in NMC811(D) in cell 2 at various OCP of the electrode (E) against Li/Li$^+$ derived from the GITT with data selection interval 5–40 s and 50–150 s, the ICI method with data selection interval 0.2–5 s and the EIS fitting ($k = \sigma\sqrt{8/\pi}$, σ: Warburg coefficient).

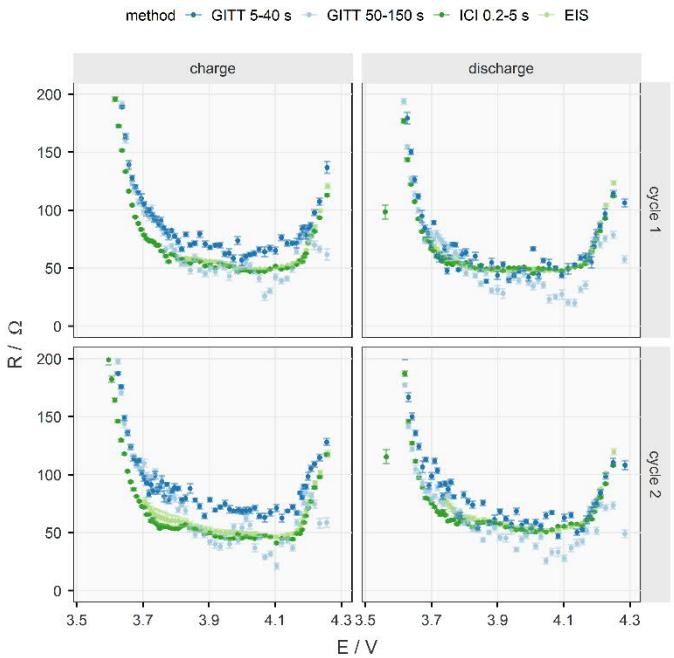

Figure S12. The internal resistance (R) of NMC811in cell 1 at various OCP of the electrode (E) against Li/Li$^+$ derived from the GITT with data selection interval 5–40 s and 50–150 s, the ICI method with data selection interval 0.2–5 s and the EIS fitting (R0+R1+R2).

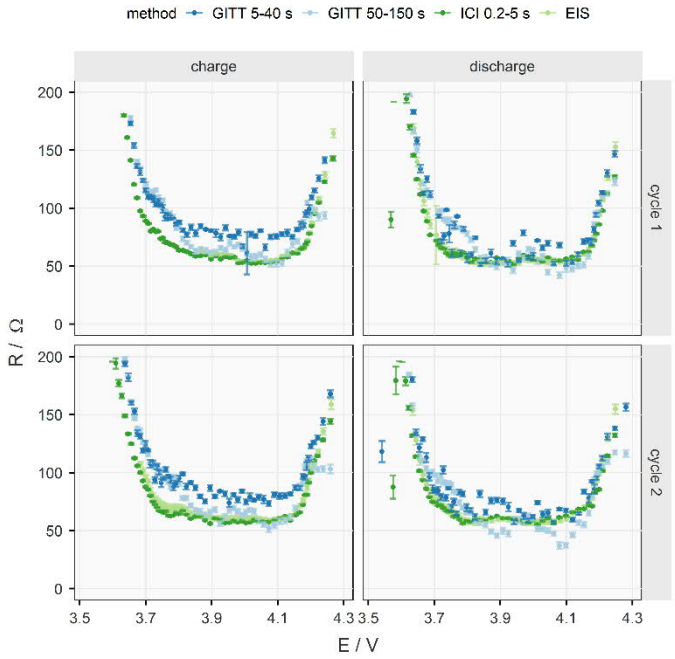

Figure S13. The internal resistance (R) of NMC811 in cell 2 at various OCP of the electrode (E) against Li/Li$^+$ derived from the GITT with data selection interval 5–40 s and 50–150 s, the ICI method with data selection interval 0.2–5 s and the EIS fitting (R0+R1+R2).

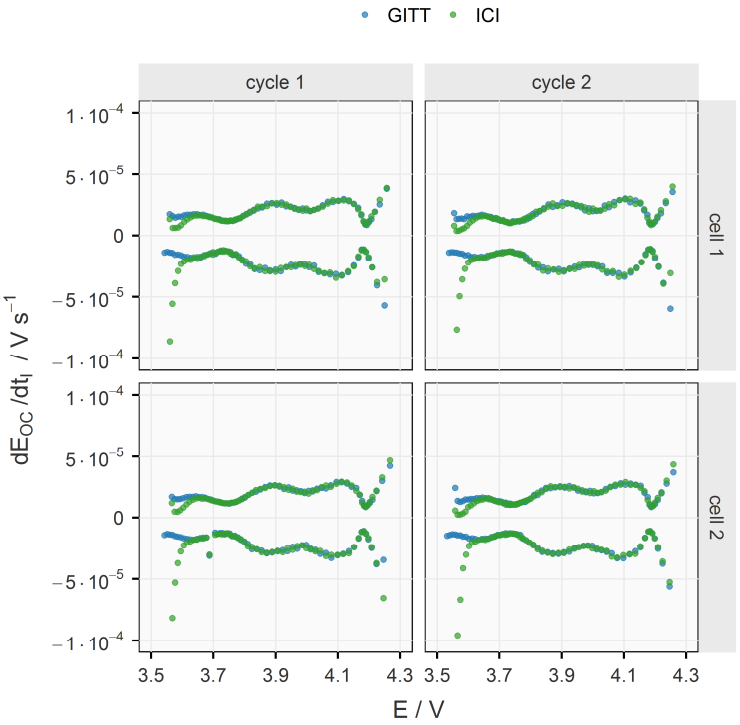

Figure S14. Comparison of the two sources of the OCP slope (dE_{OC}/dt_I): relaxed potentials of the GITT (GITT) and iR-corrected pseudo-OCP provided by the ICI method (ICI).

7. Analysis of the *operando* X-ray diffraction (XRD) results

7.1 Details of *operando* XRD measurement

The XRD experiment was carried out using a conventional Li/NMC811 pouch cell. Uniform stack pressure on the cell was ensured by fixing it between two beryllium discs. Diffraction patterns at the start and end of the *operando* run, with all the peaks ascribed to the corresponding cell components, are shown in Figure S15(a). The peaks arise from the pouch cell/separators (polyethylene and polypropylene, circles), Li metal (triangles), Al from the tabs and the pouch (square), Be discs (pentagon) and Cu tabs (hexagon). The peaks from these components do not undergo any noticeable change upon cycling. Four peaks from the rhombohedral ($R\bar{3}m$) NMC811 material (stars) are also visible. However, only the 003 reflection (~18° 2θ) is distinct and free from overlap with peaks from other cell components. Therefore, Rietveld refinements[10,11] of the NMC811 structure were carried out against the 003 reflection. As the objective of the refinements were to track the changes in the *c* lattice parameter of the $R\bar{3}m$ phase and to distinguish the "active" and the "fatigued" phases,[12] structural refinements using only the 003 reflection is sufficient. As a guide to interpreting the results from the refinements, the evolution of voltage (E) as a function of the XRD pattern no: is shown in Figure S15(b).

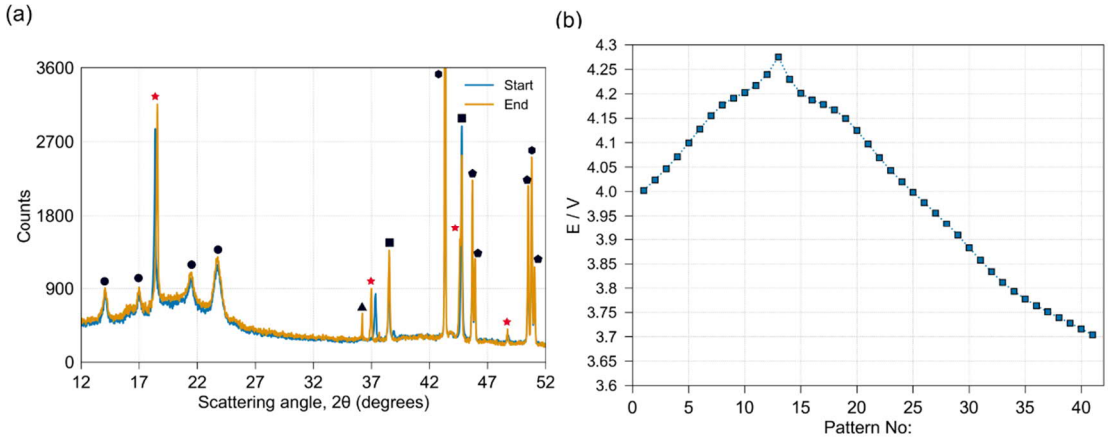

Figure S15: (a) XRD patterns at the beginning (pattern no: 1) and end (pattern no: 41) of the operando run. Peaks from NMC811 (star), pouch cell/separators (circles), Li metal (triangles), Al from the tabs and the pouch (square), Be discs (pentagon) and Cu tabs (hexagon) are highlighted. (b) Voltage of the cell as a function of the XRD pattern number.

Rietveld refinements were carried out using the Topas-Academic (V6) software.[13] A second-degree Chebychev polynomial function was used to fit the background. The profile of the 003 reflection was modeled using a Thompson-Cox-Hastings pseudo-Voigt function (*TCHZ_Peak_Type*) together with a peak asymmetry function (*Simple_Axial_Model*), to account for the

axial divergence imparted by the diffractometer setup. The latter was calibrated using a NIST Si 640c standard reference material and was fixed during the refinements. The NMC811 structure model used was similar to the one used in a previous study.[14] The peak shape functions and the refinement metrics mentioned in the following sections are defined in the Topas-Academic manual.

7.2 Single $R\bar{3}m$ phase sequential refinement

Results from the sequential Rietveld refinements of the $R\bar{3}m$ NMC811 phase are shown in Figure S16(a). In the top panel, the R_{wp} (R-weighted pattern) and GoF (Goodness of fit) values are shown, where it is seen that these metrics increase substantially between pattern numbers 10–17. The bottom panel shows the evolution of *c* lattice parameter. Here, the expected trend of shrinking *c* at high SoC and the recovery upon discharging is seen. Note that, in certain cases, the estimated standard deviation is large due to the poor fit of the model to the data. This is further evidenced in Figure S16(b) where two patterns at the end of charge (scans 13 and 14) are compared to ones before (scan 10) and after (scan 17). It is clearly seen that scans 13 and 14 are composed of more than one phase.

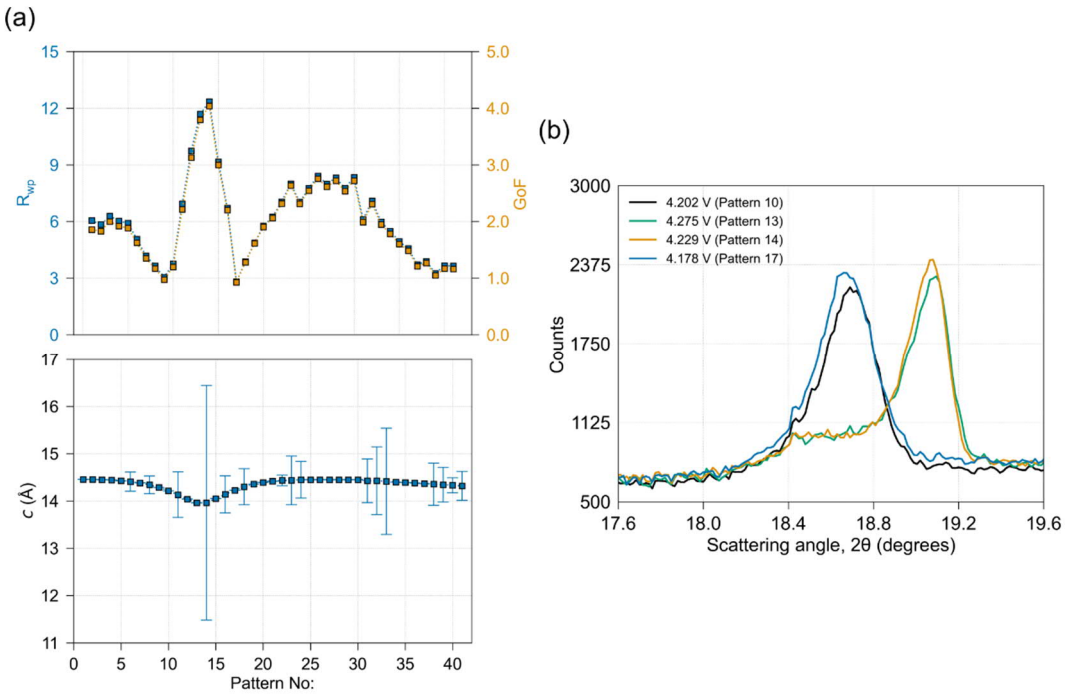

Figure S16: (a) R_{wp} and GoF values (top) and *c* lattice parameters from the sequential refinements. (b) XRD patterns at the end of charge compared to the ones before and after it.

7.3 Dual $R\bar{3}m$ phase refinement of the 003 reflection

To confirm the presence of the “active” and “fatigued” $R\bar{3}m$ phases as reported by Xu et al.,[12] Rietveld refinement of two phases against the 003 reflection from patterns 10–17 were carried out. Here, it is seen that an improved fit is obtained.

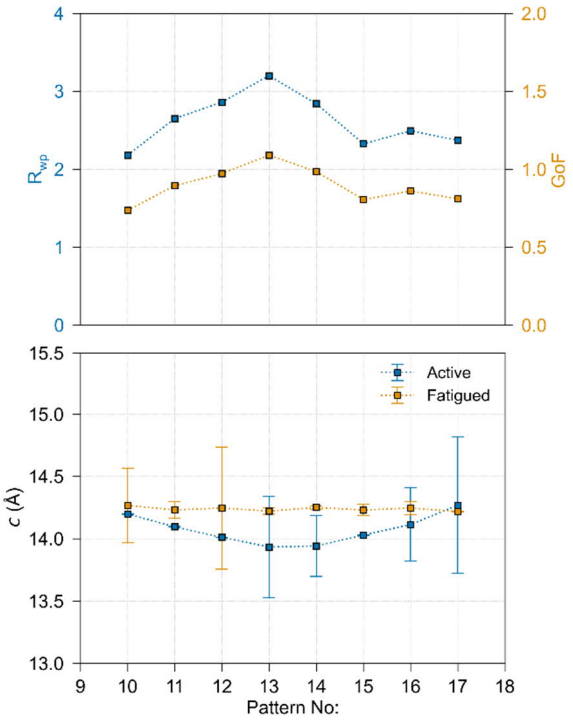

Figure S17: Rwp and GoF values (top) and evolution of *c* lattice parameters of the active and fatigued R$\bar{3}$m phases (bottom).

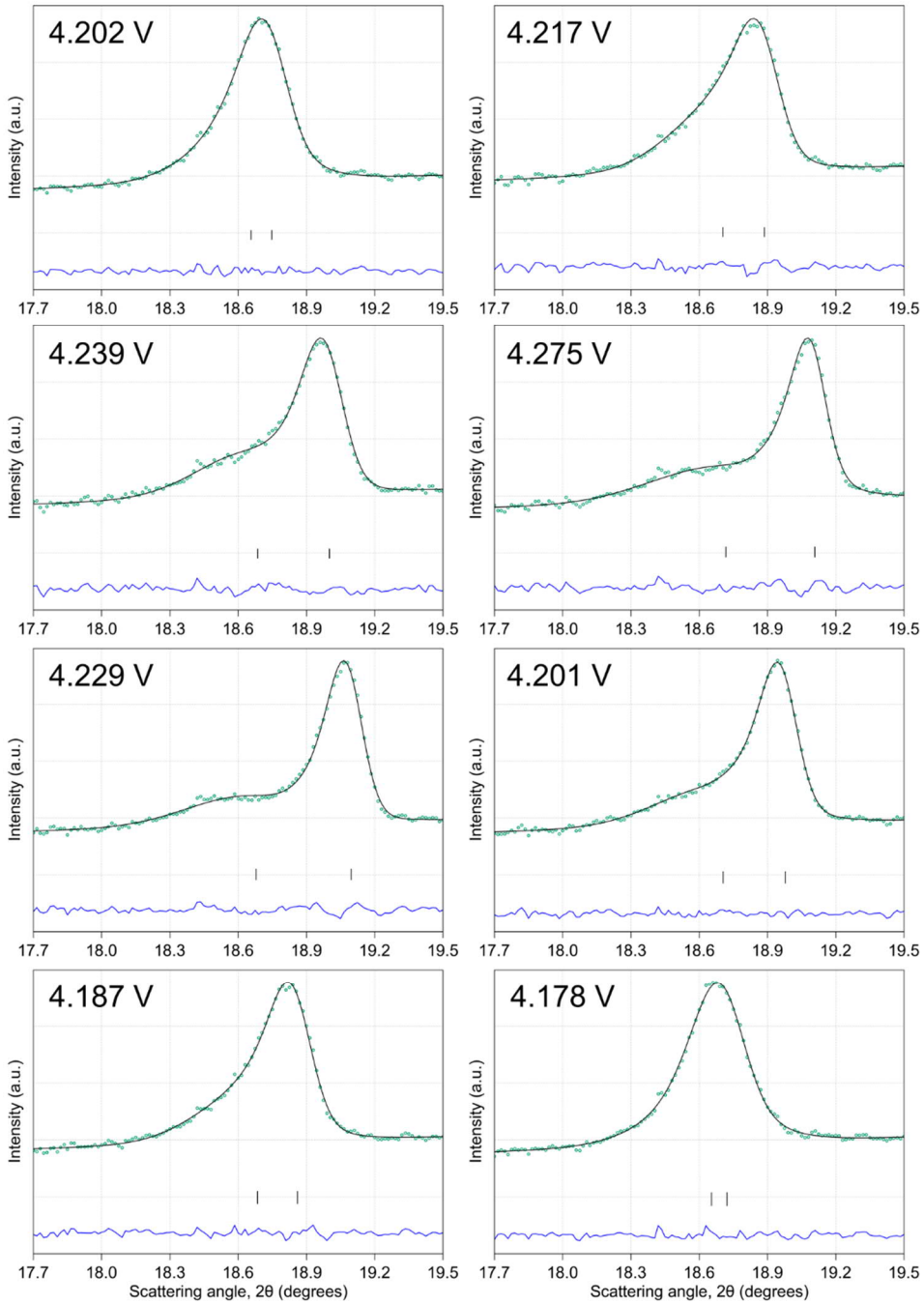

Figure S18: Rietveld refinement plots corresponding to patterns 10 to 17. The electrode potential during the measurement of each pattern is shown at the top-left corner.

References

(1) Carslaw, H. S.; Jaeger, J. C. *Conduction of Heat in Solids*, 2nd ed.; Oxford science publications; Clarendon: Oxford, 1986.

(2) Subramanian, V. R.; Ritter, J. A.; White, R. E. Approximate Solutions for Galvanostatic Discharge of Spherical Particles I. Constant Diffusion Coefficient. *J. Electrochem. Soc.* **2001**, *148* (11), E444.

(3) Liu, S. An Analytical Solution to Li/Li^+ Insertion into a Porous Electrode. *Solid State Ionics* **2006**, *177* (1–2), 53–58.

(4) Subramanian, V. R.; White, R. E. New Separation of Variables Method for Composite Electrodes with Galvanostatic Boundary Conditions. *J. Power Sources* **2001**, *96* (2), 385–395.

(5) Nickol, A.; Schied, T.; Heubner, C.; Schneider, M.; Michaelis, A.; Bobeth, M.; Cuniberti, G. GITT Analysis of Lithium Insertion Cathodes for Determining the Lithium Diffusion Coefficient at Low Temperature: Challenges and Pitfalls. *J. Electrochem. Soc.* **2020**, *167* (9), 090546.

(6) Delacourt, C.; Ati, M.; Tarascon, J. M. Measurement of Lithium Diffusion Coefficient in Li_yFeSO_4F. *J. Electrochem. Soc.* **2011**, *158* (6), A741.

(7) Shaju, K. M.; Subba Rao, G. V.; Chowdari, B. V. R. Influence of Li-Ion Kinetics in the Cathodic Performance of Layered $Li(Ni_{1/3}Co_{1/3}Mn_{1/3})O_2$. *J. Electrochem. Soc.* **2004**, *151* (9), A1324.

(8) Charbonneau, V.; Lasia, A.; Brisard, G. Impedance Studies of Li^+ Diffusion in Nickel Manganese Cobalt Oxide (NMC) during Charge/Discharge Cycles. *J. Electroanal. Chem.* **2020**, *875*, 113944.

(9) Chien, Y.-C.; Liu, H.; Menon, A. S.; Brant, W. R.; Brandell, D.; Lacey, M. J. Supporting Data for "A Fast Alternative to the Galvanostatic Intermittent Titration Technique." https://doi.org/10.5281/zenodo.4964674.

(10) Rietveld, H. M. Line Profiles of Neutron Powder-Diffraction Peaks for Structure Refinement. *Acta Crystallogr.* **1967**, *22* (1), 151–152.

(11) Rietveld, H. M. A Profile Refinement Method for Nuclear and Magnetic Structures. *J. Appl. Crystallogr.* **1969**, *2* (2), 65–71.

(12) Xu, C.; Märker, K.; Lee, J.; Mahadevegowda, A.; Reeves, P. J.; Day, S. J.; Groh, M. F.; Emge, S. P.; Ducati, C.; Layla Mehdi, B.; Tang, C. C.; Grey, C. P. Bulk Fatigue Induced by Surface Reconstruction in Layered Ni-Rich Cathodes for Li-Ion Batteries. *Nat. Mater.* **2021**, *20* (1), 84–92.

(13) Coelho, A. A. TOPAS and TOPAS-Academic: An Optimization Program Integrating Computer Algebra and Crystallographic Objects Written in C++: An. *J. Appl. Crystallogr.* **2018**, *51* (1), 210–218.

(14) Liu, H.; Naylor, A. J.; Menon, A. S.; Brant, W. R.; Edström, K.; Younesi, R. Understanding the Roles of Tris(Trimethylsilyl) Phosphite (TMSPi) in $LiNi_{0.8}Mn_{0.1}Co_{0.1}O_2$ (NMC811)/Silicon–Graphite (Si–Gr) Lithium-Ion Batteries. *Adv. Mater. Interfaces* **2020**, *7* (15), 2000277.